


Equation of state, ionic structure, and phase diagram of warm dense krypton

Zhao-Qi Wang^{1,2}, Zhi-Guo Li², Yu-Feng Wang², Lei Liu^{1,2}, Yun-Jun Gu², Qi-Feng Chen^{2,*} and Xiang-Rong Chen^{1,†}

¹College of Physics, Sichuan University, Chengdu 610065, People's Republic of China

²National Key Laboratory for Shock Wave and Detonation Physics Research, Institute of Fluid Physics, Chinese Academy of Engineering Physics, Mianyang 621900, People's Republic of China

 (Received 26 June 2019; revised manuscript received 28 August 2019; published 30 September 2019)

Extensive quantum molecular dynamics (QMD) simulations are performed to determine the equation of state, sound velocity, and phase diagram of middle- Z krypton in a warm dense regime where the pressure (P) is up to 300 GPa and the temperature is up to 60 kK. The shock wave experimental data are used to validate the present theoretical models. It is found that, within the regime of the current density (ρ) and temperature (T), sound velocity can effectively discriminate differences between different theoretical models, and therefore it is more suitable as a benchmark to verify the practicability of models. The QMD-simulated results of the ionic structures and electronic properties imply the occurrence of two kinds of phase transitions, including transition from a solidlike to fluid state and that from an insulator to conductive fluid in this T - P regime. The calculated electrical conductivities confirm that the metallization transition occurs at about 60 GPa and 17.5 kK along the principal Hugoniot. With the help of simulation results and experimental data, a comprehensive phase diagram for krypton is constructed by using the solid-fluid and insulator-metal fluid phase boundaries, which fills the gap of the experimental work [Proc. Natl. Acad. Sci. USA **112**, 7925 (2015)]. These results will provide an instructive basis for the experimental investigations of rare gases over a wide T - P range.

DOI: [10.1103/PhysRevE.100.033214](https://doi.org/10.1103/PhysRevE.100.033214)

I. INTRODUCTION

Theoretical prediction of thermophysical properties of warm dense matter (WDM) has provided new insights into our understanding of a large variety of high-energy density physics processes [1,2]. As a simple single-atom molecule with filled-shell electronic configuration, rare gases are usually used as ideal cases to study the thermophysical behavior of materials in WDM regions, such as the equation of state (EOS) [3–6] and metallization transition [1,7–10]. The available experiments have demonstrated that these properties of rare gases will change significantly [5,11–15] under shock compression and laser heating. A prominent example is that the metallization pressure of solid xenon is minimum from helium to xenon [9,16], which is one thousandth of that of neon [17,18] and is 1% that of helium [2]. Up to now, research into the thermophysical properties of helium [2,8,19,20], neon [3,18], argon [10], and xenon [5,16] under extreme conditions has gotten wide attention, but many fundamental questions about krypton, such as the compressibility, gap closure, and insulator-metal transition (IMT), are unresolved. Also, the relativistic core and d electrons of krypton at extreme conditions pose additional challenges for the current theories [5]. Therefore, it is of great interest to know whether or not krypton would have dynamics behaviors mentioned above from a theoretical point of view.

On experimental investigations, both the explosive compression technique [21] and Z machine experiment [22] are devoted to producing high-precision EOS data of fluid krypton to verify the theoretical models. These experimental data are either lower than 90 GPa or higher than 344 GPa, which are beyond the boundary of IMT and cannot accurately reveal the IMT range of fluid krypton. Moreover, the recent experiments with the laser-heated diamond anvil cell focus on the establishment of phase diagrams of dense rare gases at temperatures of 4000–15 000 K and pressures of 15–52 GPa [1], while ignoring the exploration of the metallization behavior of krypton. More importantly, the general understanding of the ionic structure and electronic character of dense krypton in high ρ - T region remains to be further improved, which will affect the development of the nuclear reactors [23]. Thus, there is a prompt need for studying these behaviors of krypton under extreme conditions.

In this paper, we perform extensive QMD simulations to determine the EOS and sound velocity of fluid krypton in the WDM regime and to verify the validity of the Perdew, Burke, and Ernzerhof (PBE) [24] exchange-correlation (XC) functional and existing chemical models. The ionic structure analysis, effective coordination number (ECN) model [25], and electronic density of state (DOS) are employed to capture the specific structural information of the system for further analysis of phase transition process. Finally, we derive the electronic conductivity from the Kubo-Greenwood formula [26,27], which is compared with previous data to locate the IMT scope and construct the phase diagram. The present theoretical results, including EOS, ionic structure, gap closure, and IMT, fill a gap in research on the thermophysical properties

*chenqf01@gmail.com

†xrchen@scu.edu.cn

[1,21] and give a clear picture about the phase diagram of dense krypton.

II. COMPUTATIONAL METHOD

The QMD simulations are implemented by the Vienna *ab initio* simulation package [28] code within the framework of the projected augmented wave method [29]. The PBE generalized-gradient approximation [24] XC potential is adopted. The $4s$ and $4p$ electrons are explicitly treated as valence electrons. The simulations are performed with a canonical ensemble where the temperature, volume of the simulation box, and particle number in the cubic box are conserved quantities. The ionic temperature is controlled by the Nosé-Hoover thermostat [30], and the electronic temperature is regulated by the Fermi-Dirac distribution [31]. To obtain well-converged pressures and energies, the tests of finite-size effects are carried out with cells containing 32, 64, and 128 atoms, respectively. The results show that the calculated pressures and total energies with a different number of atoms change very little, and the deviations of pressures and total energies between 64 and 128 atoms are within 0.3% and 0.2%, respectively. Thus, 64 krypton atoms with 512 electrons are used in our simulation. The wave functions are expanded up to a cutoff energy of 800 eV so that the total energy converges to 10^{-5} eV/atom. The periodic boundary conditions are enforced, and the Brillouin zone is sampled by using the Baldereschi zone-average point [32], $k = (1/4, 1/4, 1/4)$. Meanwhile, convergence tests up to $2 \times 2 \times 2$ uniform k -point meshes are carried out, and the results show that the Baldereschi meshes lead to sufficient convergence of the pressure and total energy with the error of 0.3% and 0.5%, respectively, over a wide range of densities and temperatures. The MD time step is set to 0.25–0.5 fs according to different densities and temperatures. The total simulation time is 5 ps, and the last 1 ps is used to run for averages of the thermodynamic quantities. Moreover, $7 \times 7 \times 7$ denser Monkhorst-Pack k -points are adopted to calculate the electronic structure with at least 10 uncorrelated snapshots in the last 1 ps, and the Fermi-Dirac distribution with electronic temperature equal to the ionic temperature is used to consider the temperature effect on electrons. For comparison, the calculation of electronic structure is also implemented by the HSE06 [33] functional with the same k -points.

III. RESULTS AND DISCUSSION

A. Equation of state and sound velocity

Based on the V - T - P - E data, we determine the Hugoniot curve of fluid krypton from the Rankine-Hugoniot relation,

$$E - E_0 = (P + P_0)(V_0 - V)/2, \quad (1)$$

where E_0 , P_0 , and V_0 are the initial internal energy, pressure, and volume, respectively; E , P , and V are the corresponding parameters of the final state. The initial condition corresponds to that of fluid krypton in the shock compression experiment (2.43 g/cm^3 and 118 K) [21,22]. In Fig. 1 we compare our results with shock compression experiments of Glukhodedov *et al.* [21], the QMD calculations with standard (AM05_8e) and improved (AM05_18e) AM05 functional by Mattsson

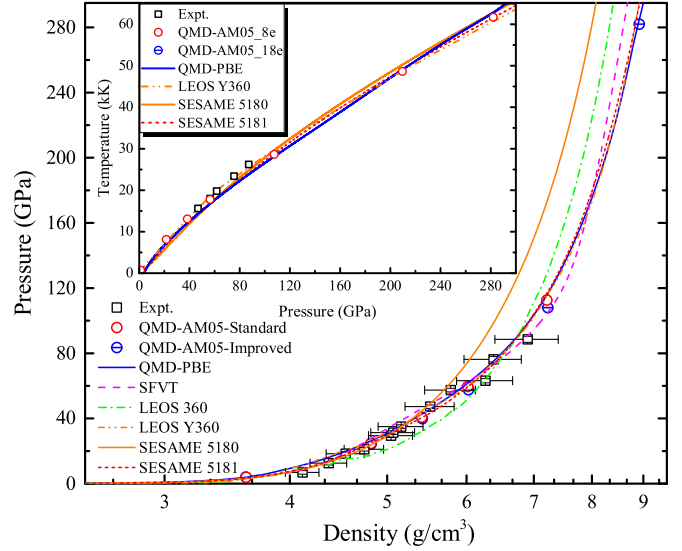


FIG. 1. Hugoniot curve for fluid krypton: our QMD-PBE results are compared with the shock compression experiment [21], QMD results with standard and improved AM05 XC functional [22], and five chemical models (SFVT [34], LEOS 360, LEOS Y360 [22], SESAME 5180, and SESAME 5181 [35]). The SFVT model with the consideration of dissociation is shown by the magenta dotted line. The inset gives the temperature as a function of the pressure along the principal Hugoniot.

et al. [22], and five chemical models [34,35]. For the QMD results, the PBE functional can well reproduce the experimental ρ - P data within the error bars up to 90 GPa and is in accord with the results from the AM05 functional up to 300 GPa. For the chemical models, the results from the self-consistent fluid variational theory (SFVT), LEOS Y360, and SESAME 5181 are in agreement with the experimental Hugoniot data however, LEOS 360 and SESAME 5180 obviously overestimate the pressure and give stiffer results deviating from the experiments. The differences among chemical models may mainly arise from the different treatments of the electronic contributions in the Helmholtz free energy [22]. For example, the SFVT is a multicomponent chemical equilibrium model considering the lowering of ionization of dense krypton [34], and thus it can give a satisfying prediction for the Hugoniot curve. In the inset of Fig. 1, the principal Hugoniot in the T - P plane [21] is depicted. The QMD results agree with the experimental data with an error lower than 8%. Also, the PBE and AM05 results show good agreements with deviations not exceeding 1.5%. This suggests that both of them can reasonably describe the EOS of fluid krypton in the current T - P regime.

As mentioned in Ref. [36], the sound velocity is another crucial variable to benchmark the theoretical models. Since the sound velocity is the second derivative of the free energy, it is more sensitive to subtle differences among different theoretical models [37]. We calculate the bulk sound velocity along the principal Hugoniot according to the P - V relation [38], $C_b = \sqrt{K_T(1 + \alpha\gamma T)}/\rho$, where $K_T = -V(dP/dV)_T$ means the isothermal bulk modulus, α the thermal expansion coefficient, γ the Grüneisen parameter, T the temperature, and ρ the mass density. Figure 2 and the inset summarize the calculated bulk sound velocity as a function of density and

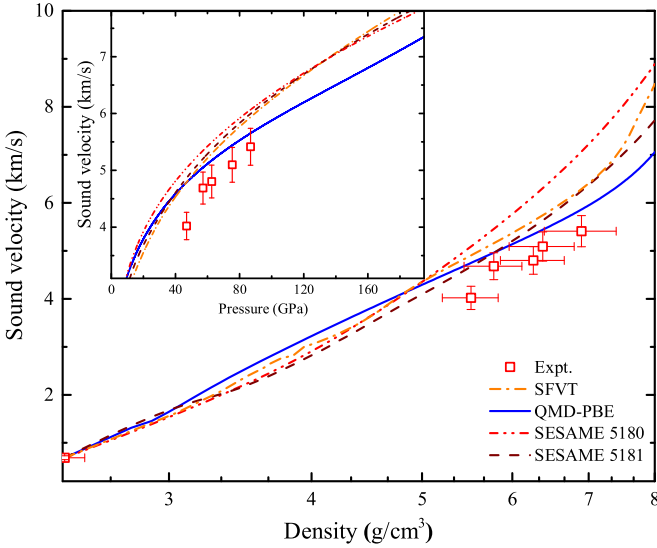


FIG. 2. The bulk sound velocity as a function of the density and pressure, respectively, from our QMD-PBE simulation, chemical models (SFVT, SESAME 5180 and SESAME 5181 [35]), and experiment results [21], along the principal Hugoniot.

pressure, respectively. Compared with experimental results [21], our results calculated by the PBE functional predict a slightly higher sound velocity curve but show a better agreement with experiment than chemical models of SFVT and SESAME, especially for densities above $\sim 5.8 \text{ g/cm}^3$. On the other hand, the results between the chemical models and experiments show distinct deviations, and the deviations become larger with increasing density. One primary cause for this deviation may be the approximation that various species interacting via effective pair potentials in chemical models lose effectiveness when the density becomes higher due to more complex many-body interaction in the high densities. [6] As mentioned, the differences of the Hugoniot curves among PBE, SFVT, and SESAME 5181 calculations are small. However, the differences are obviously enlarged for the case of sound velocity. This indicates that the sound velocity may be more suitable as a benchmark to verify the practicability of theoretical models. On the other hand, this also suggests that the PBE functional can reasonably reproduce the experimental

EOS and sound velocity, which ensures the reliability of the following predictions for structures and electronic properties of dense krypton.

B. Ionic structure and solid-fluid transition

The transition of condensed matter between a solid state and fluid state is a topic of wide scientific interest [39], and it can be qualitatively observed by the ionic structure analysis. Therefore, we carefully examine the ionic structures of dense krypton with the pair distribution function (PDF) to give insight into details of the phase transitions in the current T - P regime. The obtained PDFs for density of 2.617 , 5.328 , and 8.0 g/cm^3 at different temperatures are presented in Fig. 3. At the lower density of 2.617 g/cm^3 in Fig. 3(a), the PDF of 1 kK exhibits one obvious peak around 3.66 \AA , which indicates a short-range ordered fluid state. The peaks are lowered with increasing temperature. When $T > 10 \text{ kK}$, the peaks gradually disappear and the system is a disordered atomic fluid. For the middle density of 5.328 g/cm^3 in Fig. 3(b), the second peak is gradually obvious at $T < 2.5 \text{ kK}$. For the higher density of 8.0 g/cm^3 in Fig. 3(c), two distinct peaks exist in the PDFs at $T < 5.0 \text{ kK}$. When the temperature increases up to 10 kK , the second peaks gradually disappear and the solidlike krypton turns into a short-range ordered fluid state. With further increasing temperature, all peaks gradually disappear. These indicate that the high temperature will destroy the long-range order in the solidlike krypton and the short-range order in the fluid krypton. In conclusion, krypton undergoes a transition from the solidlike to fluid state below 5 kK in density ranges from 2.617 to 8.0 g/cm^3 , which is very close to the melting curves of solid krypton [14]. This melting curve has been clearly presented later in this paper (see Fig. 7 below) to determine the solid-fluid phase boundary of krypton.

To analyze this transition in more detail, we employ the ECN model [25] to capture the structural information of the system from the perspective of ionic aggregative distribution. This model takes into account that a particular atom i is surrounded by the neighbor atoms within a specific distance and then classifies these local structures into single, chain, circle, and cluster (see Table I caption for an explanation) by counting the number of atoms surrounding atom i with a bond length smaller than the specific distance. The detailed

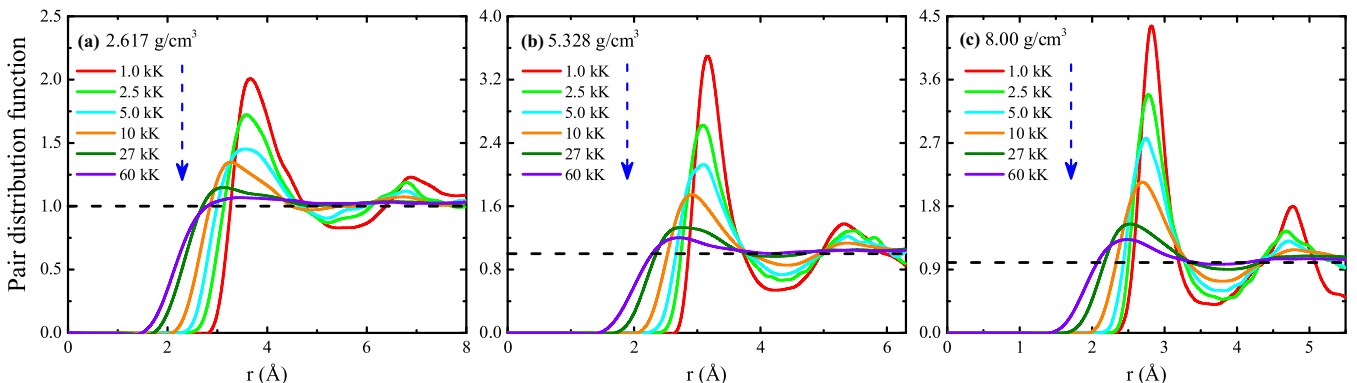


FIG. 3. The PDF of dense krypton along three isochores with densities of (a) 2.617 g/cm^3 , (b) 5.328 g/cm^3 , and (c) 8.00 g/cm^3 at different temperatures. The first peaks of the PDF are arranged from high to low along the direction of the blue dashed-line arrow.

TABLE I. The temperature dependence of the cluster fraction for krypton at different densities with the ECN model based on the QMD-PBE simulations. Single represents the structures with a single atom. Chain represents the chain structure with every atom except the first and last atom of the chain has only two nearest atoms. Circle represents the circle structure with every atom in the structure owning only the two nearest atoms in a circle. Cluster represents a complex structure whose central atom has more than three nearest atoms.

ρ (g/cm ³)	T (kK)	Single (%)	Circle (%)	Chain (%)	Cluster (%)
2.617	1.0	64.0	1.20	0.00	34.8
	10	77.6	5.50	0.10	16.8
	60	85.6	7.40	0.30	6.70
5.328	1.0	95.1	0.10	0.00	4.80
	10	71.9	1.40	0.00	26.7
	60	82.9	7.10	0.10	9.90

categorizing method for ionic structures can be found in Ref. [40]. The ECN is described by the following set of equations:

$$\text{ECN} = \frac{1}{N} \sum_{i=1}^N \text{ECN}_i = \frac{1}{N} \sum_{i=1}^N \sum_{j \neq i} \exp \left[1 - \left(\frac{d_{ij}}{d_{av}^i} \right)^6 \right], \quad (2)$$

$$d_{av} = \frac{1}{N} \sum_{i=1}^N d_{av}^i, \quad (3)$$

$$d_{av}^i = \frac{\sum_j d_{ij} \exp \left[1 - \left(\frac{d_{ij}}{d_{av}^i} \right)^6 \right]}{\sum_j \exp \left[1 - \left(\frac{d_{ij}}{d_{av}^i} \right)^6 \right]}, \quad (4)$$

where i and j are the indices of krypton atoms, d_{ij} is the distance between the i th and j th atoms, N the total number of atoms in the system, and d_{av} the average value of the effective bonding diameter for a particular configuration including the temperature and density effects. We define the specific distance as the average bond length d_{av} . Previous researchers [41–44] have confirmed that this model provides a more clear approach to identify the possible structural trend of the system in WDM. The statistical average for the component after thermalization is displayed in Table I. For the density of 2.617 g/cm³, the percentage of a single atom occupies 64% at 1 kK. As the temperature rises, this percentage is always increasing and it goes up to 85.6% at 60 kK. This monotonous rise in temperature may suggest that the system is continually dissociatively driven by the temperature effect in this temperature range, which is consistent with the previous discussion of the PDF. For the middle density of 5.328 g/cm³, the percentage of a single atom is 95.1% at 1 kK, and it first goes down to 71.9% at 10 kK, and then it goes up to 82.9% at 60 kK. This descending character also exists in higher densities. With the help of the melting curve of solid krypton [14], we interpret the decrease of the percentage of a single atom as an indication that the transition from a solidlike to fluid state occurs in this range. The specific process may be as follows: at low temperature of 1 kK, the system is a monoatomic molecular solidlike state, the solidlike krypton first melts into

fluid and partially forms a cluster with the rise of temperature, then the clusters in the fluid state dissociate driven by the temperature effect with further increasing temperature. This behavior of the ECN with temperature and density sufficiently illustrates the phase transition from solidlike krypton to a fluid state, which confirms the conclusions from the PDF.

C. Electronic density of state and gap closure

It is well known that the IMT in WDM regime is an essential phenomenon to understand the thermophysical properties of highly compressed condensed matter. Here we use the DOS to directly observe this behavior of dense krypton. The thermally occupied DOSs of dense krypton at 2.617, 5.328, and 8.0 g/cm³ obtained by the PBE and HSE06 XC functional are exhibited in Fig. 4. At lower temperature (1 kK), one can clearly see that the two higher peaks of DOSs are composed of the atomic 4s and 4p states, followed by a gap at the Fermi energy, which is then followed by a continuous spectrum of conducting states. With the increase of density, the band gap of dense krypton at 1 kK first increases and then decreases, from 5.54 eV at 2.617 g/cm³ to 6.21 eV at 5.328 g/cm³, then to 4.02 eV at 8.0 g/cm³ [see Figs. 4(a), 4(c), and 4(e)]. This trend is also found in the fluid He [20,45] and Ne [7]. It is probably because the delocalization effect of electrons is weaker than the repulsion effect of electrons induced by pressure in the range of 2.43–5.5 g/cm³ (see Fig. 5), the band gaps therefore increase with the increase of density [7]. At higher densities, the delocalization effect gradually dominates, resulting in a gradual decrease in band gap. For all densities, the band gap of dense krypton is close to 0 when the temperature is over 10 kK. On the other hand, we also find that the peaks at the top of the valence band broaden and merge with the increase of temperature, due to the thermal excitation of electron and the increased admixture of s -like and p -like states. Note that the values of band gap depend on the XC functional used in the density functional theory (DFT) calculation, and the PBE functional is known to underestimate the band gap. To address this concern, we use the HSE06 functional [see Figs. 4(b), 4(d), and 4(f)] to give a more reasonable band gap. Our results show that the band gaps obtained by the HSE06 functional are ~ 1.5 eV higher than the values of the PBE functional. But the evolution tendency of the band gap with density or temperature by using the PBE is consistent with that of the HSE06 functional and is reliable for qualitative comparison.

In order to further quantify the variation characteristics of gap closure in this ρ - T regime, we give the band gap of krypton along several different isotherms in Fig. 5, and the band gaps of solid krypton with the face-centered cubic (fcc) at 0 K are also given for comparison. The calculated results of the fcc phase by using PBE functional at 0 K is well consistent with the theoretical values of Kwon *et al.* [13], which justifies our theoretical calculation. Furthermore, the ρ - T dependence of the gap closure is an important reference factor for designing experiments. As Soubiran *et al.* [20] suggested, we assume initially a density- and temperature-dependent formula, $E_g = E_0 - [A_0 + A_1(T/T_0)](\rho/\rho_{0L}) - B(T/T_0)$, where $kT_0 = 14.00$ eV and $\rho_{0L} = 2.43$ g/cm³. The fit region spans a wide range of densities from 2.43 to 14.5 g/cm³ and

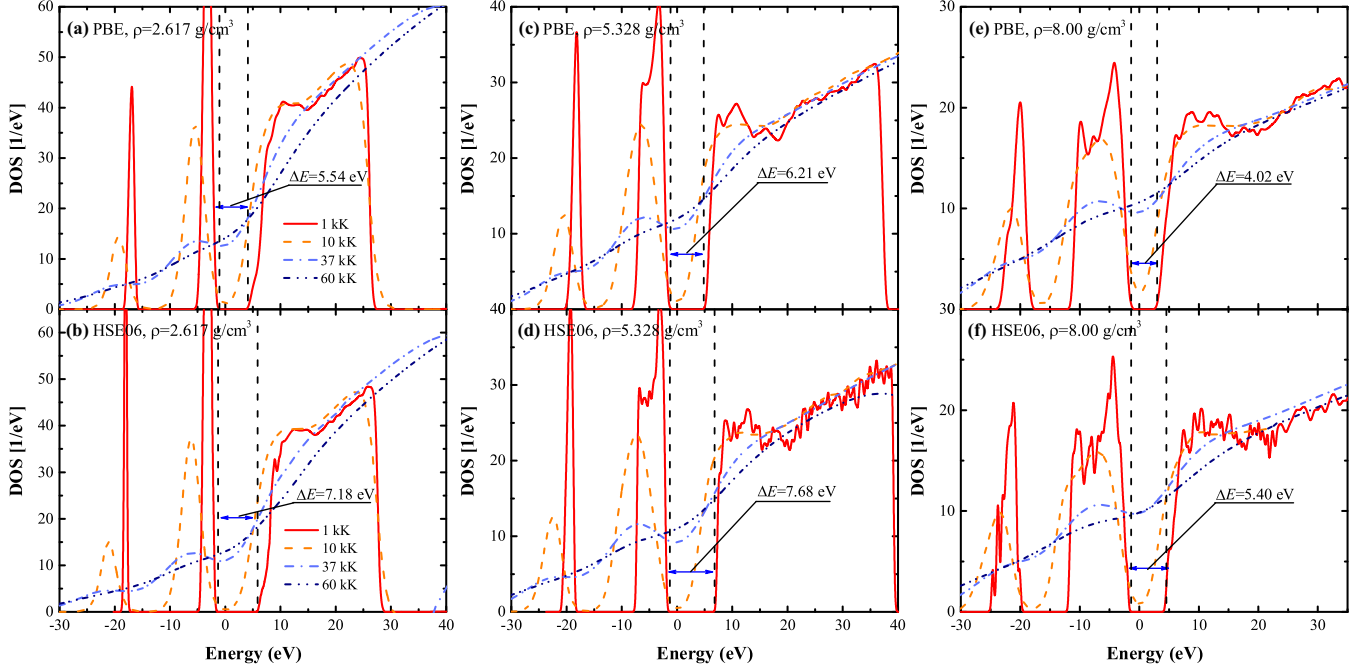


FIG. 4. Electronic density of state of dense krypton by using the PBE [(a), (c), and (e)] and HSE06 [(b), (d), and (f)] XC functional with densities of 2.617, 5.328, and 8.00 g/cm³. The band gaps of dense krypton at 1 kK are marked, and the Fermi energy is shifted to zero.

temperatures from 0 to 10 kK. The best fit parameters obtained by the PBE functional yield $E_0 = 9.85$ eV, $A_0 = 1.75$ eV, $A_1 = -33.66$ eV, and $B = 305.99$ eV, and those obtained by the HSE06 functional yield $E_0 = 11.81$ eV, $A_0 = 1.87$ eV, $A_1 = -36.90$ eV, and $B = 280.71$ eV. With the help of this formula, we conclude that the metallization density of krypton by using the PBE (HSE06) functional

is 13.6(14.1) g/cm³ at 0 K, 12.5(13.5) g/cm³ at 1000 K, and 10.1(12.0) g/cm³ at 2500 K. This formula can directly reproduce almost all our calculated band gap of krypton and fill the gap of recent work by McWilliams *et al.* [1]. Also, the metallization process of krypton can be examined with the Herzfeld-Goldhammer picture [46]. For compression systems, its dielectric catastrophe and a transition to a metallic state satisfy the relationship $4\pi\alpha D/3 = 1$, where α and D represent the average electronic polarizability and molar density, respectively. The average electronic polarizability of krypton is 2.4844×10^{-24} cm³ [47], so the metallization density is predicted to occur around 13.376 g/cm³, which is in excellent accord with the value of our first-principles calculation. This also documents the rationality of the fit parameters obtained by the above fitting formula.

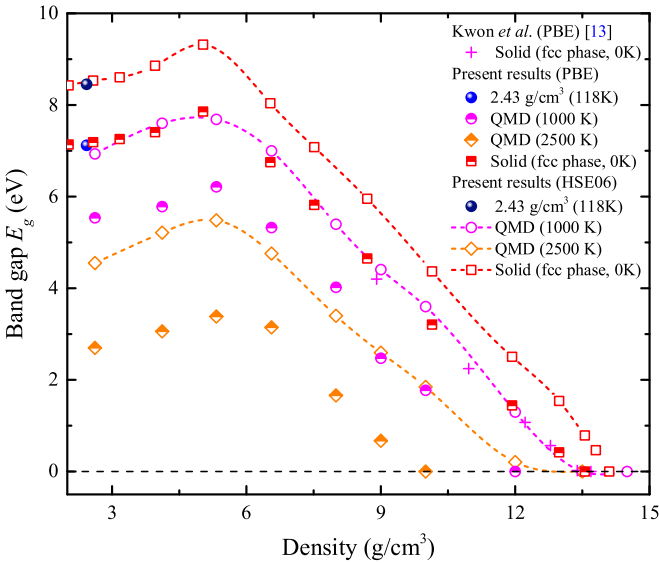


FIG. 5. Band gap of krypton at an initial fluid point, compared with QMD results along 1000 and 2500 K isotherms calculated by the PBE and the HSE06 functionals with $7 \times 7 \times 7$ k -points; the theoretical results for the fcc solid krypton at 0 K calculated with $21 \times 21 \times 21$ k -points and the first-principles calculation by Kwon *et al.* [13].

D. Insulator-metal transition and phase diagram

The study of the IMT of a substance during dynamic compression is of great significance to the construction of the metallization boundary and phase diagram. Here we employ the DFT method to calculate the dc conductivity on several isotherms to describe the IMT of dense krypton. The dynamics conductivity $\sigma(\omega)$ is derived from the Kubo-Greenwood formula [26,27] as

$$\sigma(\omega) = \frac{2\pi e^2 \hbar^2}{3m^2 \omega \Omega} \sum_k W(k) \sum_{j=1}^N \sum_{i=1}^N \sum_{\alpha=1}^3 [F(\varepsilon_{i,k}) - F(\varepsilon_{j,k})] \times |(\Psi_{j,k} | \nabla_{\alpha} | \Psi_{i,k})|^2 \delta(\varepsilon_{j,k} - \varepsilon_{i,k} - \hbar\omega), \quad (5)$$

where e , m , ω , and Ω are the electron charge, particle mass, frequency, and cubic supercell volume, respectively. The $W(k)$ is the k -point weight in the Monkhorst-Pack scheme. The summation over the matrix elements of the Bloch functions

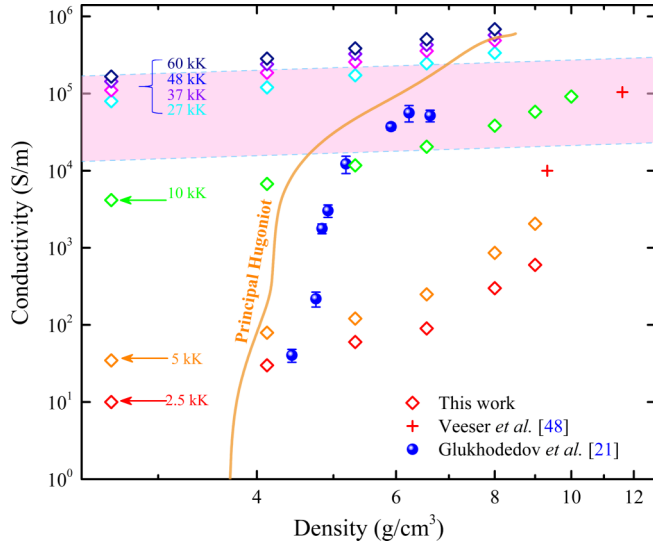


FIG. 6. The density dependence of the dc conductivity (squares) for krypton at 2.5 kK (red), 5 kK (orange), 10 kK (green), 27 kK (cyan), 37 kK (magenta), 48 kK (violet), and 60 kK (navy blue) computed with the PBE functional, compared with the experimental result of Glukhodedov *et al.* [21] and Veese *et al.* [48]. The pink region around the Mott [49] minimum metallic conductivity is used to determine the density of metallization. The orange solid line represents our calculated dc conductivity along the principal Hugoniot.

with the momentum operator ∇_{α} , weighted with the difference of the Fermi occupations $F(\varepsilon_{i,k})$, is performed over all N bands. $\Psi_{i,k}$ and $\varepsilon_{i,k}$ are the eigenstate and eigenvalue for the band i and the k point, respectively. This formula is evaluated for at least 10 uncorrelated snapshots from the last 1 ps QMD trajectories at each ρ - T condition. The optical properties are then computed using the Kramers-Kronig formula. In our computations, the δ function is replaced by a Gaussian width Δ given by the average spacing between eigenvalues weighted by the corresponding change in the Fermi function [50]. Moreover, we have carefully checked the convergence of the conductivity results. The tests of band number and k -points are carried out with bands up to 2000 and k -points up to $4 \times 4 \times 4$ meshes. The results show that the dc conductivities are almost unchanged when the band number is greater than 1000 and the sample is larger than $2 \times 2 \times 2$ meshes. Thus, the $3 \times 3 \times 3$ k -points and the 1200–2000 bands are set to yield conductivities at different densities and temperatures, which provide a good convergence of conductivity better than 2%. The average of dynamic conductivity is taken over an ensemble of configurations sampled, and the dc electrical conductivity is given as the static limit of dynamic conductivity. The rationality of this approach has been verified in many works [8,45].

We use the criterion of the minimum metallic conductivity provided by Mott [49] between $0.026e^2/(2a\hbar)$ and $0.333e^2/(2a\hbar)$ (e , a , and \hbar are the elementary charge, interatomic distance, and reduced Plank constant, respectively) to distinguish between the insulating and metallic behavior of fluid krypton. In Fig. 6 the present results are compared with shock compression experiments of Glukhodedov *et al.* [21] and Veese *et al.* [48]. We note that the experimental

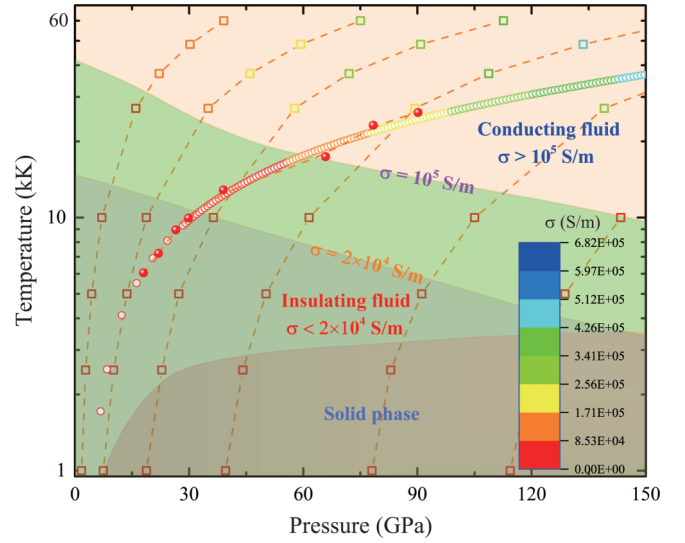


FIG. 7. Phase diagrams of krypton from the calculated (squares) and experimental (sphere) data [21]. The insulating fluid is defined as $\sigma < 2 \times 10^4$ S/m and conducting fluid as $\sigma > 10^5$ S/m. The squares refer to the conductivity along seven isochores of 2.617, 4.119, 5.328, 6.56, 8.0, and 9.0 g/cm³, the circles represent the dc conductivity along the principal Hugoniot, and the value of conductivity is shown by color with the color bar. The melting curve of solid krypton [14,15] is also used to define phase boundaries between the solid phase and fluid phase.

data between 4.43 and 6.63 g/cm³ show a sharp increase of conductivities from 40 to 52 000 S/m, characterizing the occurrence of the insulator-to-metal transition. This character is also captured by our QMD calculation. For instance, the dc conductivity value is substantially close to 0 at a low temperature of 1 kK and density of 5.328 g/cm³, while it is up to 11700 S/m at 10 kK. We locate the IMT at about 4.63 and 6.95 g/cm³ along the Hugoniot on the lower and upper boundary in Fig. 6, respectively, which provides guidance for the design and verification of metallization experiments in the future. Moreover, we can analyze the metallic regime from the perspective of the Mott scaling parameter $n_c^{1/3} a^*$ [51], where n_c is the critical electron density and a^* is the Bohr radius of a bound electron. We find that the metallic transition (lower boundary) of monoatomic fluid krypton occurs at $n_c^{1/3} a^* \sim 0.64$, which is about a factor of 1.56 larger than the alkali metals [39]. This scaling parameter is examined by using the fluid helium data [8] and may also be applicable to other rare gas fluids.

The compression of dense krypton by using QMD calculation makes it possible to obtain physical information about an as-yet-unexplored part of phase diagram. Based on the calculated dc conductivity and experimental data [14,21], we construct an phase diagram for krypton by employing a solid-fluid and insulator-metal phase boundary, as illustrated in Fig. 7. We define the insulating fluid region as $\sigma < 2 \times 10^4$ S/m and the conducting fluid region as $\sigma > 10^5$ S/m. The boundaries of 2×10^4 S/m and 10^5 S/m are determined by fitting the calculated data with a quartic polynomial. The first part of the solid-fluid phase boundary up to 70 GPa is determined by the experimental melting curve of solid krypton

[14], and the rest from 70 to 150 GPa is obtained from the extrapolation of the melting curve of solid krypton, which is constricted by the transition interval obtained by the PDF. A previous experiment [21] has shown that the conductivity saturates at ~ 70 GPa along the Hugoniot, indicating a transition of insulators into a metallic state. The metallization pressure of our result is located at ~ 60 GPa and ~ 17.5 kK along the Hugoniot (in Fig. 7), which is consistent with shock wave experimental data, but higher than the metallization pressure measured in the solid krypton [14]. By using the metallization of lower boundary, we confirm that the transition pressure of fluid krypton is 103–108 GPa at the temperature of 3.27–4 kK, which is between that of fluid argon (~ 160 GPa at 4 kK) and that of fluid xenon (~ 60 GPa at 3.27 kK) [1]. The results of the dc conductivity and the phase boundary not only reveal a connection between the underlying ionic structure and metallization, but also provide a basis for future experimental metallization research.

IV. CONCLUSION

We perform extensive QMD simulations on middle- Z krypton to determine the EOS, sound velocity, ionic structure, and phase diagram within the warm dense region where the pressure is up to 300 GPa and the temperature is up to 60 kK. The EOS models, including the first-principles methods and chemical models, are validated using shock wave experimental data. Our results suggest that the sound velocity can effectively discriminate differences between different theoretical models, and therefore it is more suitable

as a benchmark to verify the practicability of models. By analysis of the PDF, ECN, and DOS, we find that two kinds of phase transitions, the transition from a solidlike to fluid state and that from an insulator to a conductive fluid, exist in the current T - P region. We also prove that those transitions are closely related to the evolution of ionic structure and band gap and give a ρ - T dependent formula of band gap and the electrical conductivity dependent on the Mott scaling parameter. At approximately 14.1 g/cm³, the gap closure of solid krypton emerges, which agrees well with the case of the Herzfeld-Goldhammer picture. The IMT is further identified to occur at about 60 GPa and 17.5 kK along the principal Hugoniot by the dc conductivity data. Finally, the solid-fluid and insulator-metal fluid phase boundary and phase diagram of dense krypton are constructed based on our simulation results, which provide a better understanding of the interplay between melting and metallization.

ACKNOWLEDGMENTS

This work is supported by the Foundation of National Key Laboratory of Shock Wave and Detonation Physics (Grant No. JCKYS2018212001), Science Challenge Project (Grant No. TZ2016001), National Natural Science Foundation of China (Grants No. 11872057, No. 11802280, and No. 11674292), National Postdoctoral Program for Innovative Talents (Grant No. BX201700215), and NSAF (Grant No. U1830101). We also acknowledge support for the computational resources by the TianHe-2 in the LvLiang Cloud Computing Center of China.

-
- [1] R. S. McWilliams, D. A. Dalton, Z. Konôpková, M. F. Mahmood, and A. F. Goncharov, *Proc. Natl. Acad. Sci. USA* **112**, 7925 (2015).
- [2] L. Stixrude and R. Jeanloz, *Proc. Natl. Acad. Sci. USA* **105**, 11071 (2008).
- [3] J. Tang, Y. J. Gu, Q. F. Chen, Z. G. Li, J. Zheng, C. J. Li, and J. T. Li, *Phys. Rev. B* **97**, 140101(R) (2018).
- [4] Z. G. Li, Y. Cheng, Q. F. Chen, and X. R. Chen, *Phys. Plasmas* **23**, 052701 (2016).
- [5] S. Root, R. J. Magyar, J. H. Carpenter, D. L. Hanson, and T. R. Mattsson, *Phys. Rev. Lett.* **105**, 085501 (2010).
- [6] Z. G. Li, Q. F. Chen, Y. J. Gu, J. Zheng, W. Zhang, L. Liu, G. J. Li, Z. Q. Wang, and J. Y. Dai, *Phys. Rev. B* **98**, 064101 (2018).
- [7] J. Tang, B. Y. Ao, L. Huang, X. Q. Ye, Y. J. Gu, and Q. F. Chen, *J. Chem. Phys.* **150**, 111103 (2019).
- [8] A. Kietzmann, B. Holst, R. Redmer, M. P. Desjarlais, and T. R. Mattsson, *Phys. Rev. Lett.* **98**, 190602 (2007).
- [9] K. A. Goettel, J. H. Eggert, I. F. Silvera, and W. C. Moss, *Phys. Rev. Lett.* **62**, 665 (1989).
- [10] W. Kang, S. J. Zhao, S. Zhang, P. Zhang, Q. F. Chen, and X. T. He, *Sci. Rep.* **6**, 20623 (2016).
- [11] J. Li, B. E. Bursten, B. Y. Liang, and L. Andrews, *Science* **295**, 2242 (2002).
- [12] N. Bartlett and P. R. Rao, *Proc. Chem. Soc.* (1964) 393.
- [13] I. Kwon, L. A. Collins, J. D. Kress, and N. Troullier, *Phys. Rev. B* **52**, 15165 (1995).
- [14] R. Boehler, M. Ross, P. Söerlind, and D. B. Boercker, *Phys. Rev. Lett.* **86**, 5731 (2001).
- [15] A. D. Rosa, G. Garbarino, R. Briggs, V. Svitlyk, G. Morard, M. A. Bouhifd, J. Jacobs, T. Irifune, O. Mathon, and S. Pascarelli, *Phys. Rev. B* **97**, 094115 (2018).
- [16] M. I. Eremets, E. A. Gregoryanz, V. V. Struzhkin, H.-K. Mao, R. J. Hemley, N. Mulders, and N. M. Zimmerman, *Phys. Rev. Lett.* **85**, 2797 (2000).
- [17] J. C. Boettger, *Phys. Rev. B* **33**, 6788 (1986).
- [18] K. P. Driver and B. Militzer, *Phys. Rev. B* **91**, 045103 (2015).
- [19] P. M. Celliers, P. Loubeyre, J. H. Eggert, S. Brygoo, R. S. McWilliams, D. G. Hicks, T. R. Boehly, R. Jeanloz, and G. W. Collins, *Phys. Rev. Lett.* **104**, 184503 (2010).
- [20] F. Soubiran, S. Mazevet, C. Winisdoerffer, and G. Chabrier, *Phys. Rev. B* **86**, 115102 (2012).
- [21] V. D. Glukhodedov, S. I. Kirshanov, T. S. Lebedeva, and M. A. Mochalov, *J. Exp. Theor. Phys.* **89**, 292 (1999).
- [22] T. R. Mattsson, S. Root, A. E. Mattsson, L. Shulenburg, R. J. Magyar, and D. G. Flicker, *Phys. Rev. B* **90**, 184105 (2014).
- [23] M. Lozinsek and G. J. Schrobilgen, *Nat. Chem.* **8**, 732 (2016).
- [24] J. P. Perdew, K. Burke, and M. Ernzerhof, *Phys. Rev. Lett.* **77**, 3865 (1996).
- [25] M. J. Piotrowski, P. Piquini, and J. L. F. Da Silva, *Phys. Rev. B* **81**, 155446 (2010).
- [26] R. Kubo, *J. Phys. Soc. Jpn.* **12**, 570 (1957).
- [27] D. A. Greenwood, *Proc. Phys. Soc.* **71**, 585 (1958).
- [28] G. Kresse and J. Furthmüller, *Phys. Rev. B* **54**, 11169 (1996).

- [29] G. Kresse and D. Joubert, *Phys. Rev. B* **59**, 1758 (1999).
- [30] S. Nose, *J. Chem. Phys.* **81**, 511 (1984).
- [31] N. D. Mermin, *Phys. Rev.* **137**, A1441 (1965).
- [32] A. Baldereschi, *Phys. Rev. B* **7**, 5212 (1973).
- [33] J. Heyd, G. E. Scuseria, and M. Ernzerhof, *J. Chem. Phys.* **118**, 8207 (2003).
- [34] Q. F. Chen, J. Zheng, Y. J. Gu, and Z. G. Li, *Phys. Plasmas* **22**, 122706 (2015).
- [35] A. E. Mattsson (unpublished).
- [36] D. E. Fratanduono, M. Millot, A. F. Panella, P. A. Sterne, G. W. Collins, D. G. Hicks, J. H. Eggert, T. R. Boehly, and P. M. Celliers, *Phys. Plasmas* **26**, 012710 (2019).
- [37] R. S. Hixson, D. A. Boness, J. W. Shaner, and J. A. Moriarty, *Phys. Rev. Lett.* **62**, 637 (1989).
- [38] M. Li, S. Zhang, H. P. Zhang, G. M. Zhang, F. Wang, J. H. Zhao, C. W. Sun, and R. Jeanloz, *Phys. Rev. Lett.* **120**, 215703 (2018).
- [39] M. Bastea, A. C. Mitchell, and W. J. Nellis, *Phys. Rev. Lett.* **86**, 3108 (2001).
- [40] J. Y. Dai, Y. Hou, and J. M. Yuan, *High Energy Density Phys.* **7**, 84 (2011).
- [41] D. D. Kang and J. Y. Dai, *J. Phys.: Condens. Matter* **30**, 073002 (2018).
- [42] L. Liu, Z. G. Li, J. Y. Dai, Q. F. Chen, and X. R. Chen, *Phys. Rev. E* **97**, 063204 (2018).
- [43] H. Y. Sun, D. D. Kang, J. Y. Dai, J. L. Zeng, and J. M. Yuan, *Phys. Rev. E* **89**, 022128 (2014).
- [44] J. Y. Dai, Y. Hou, D. D. Kang, H. Y. Sun, J. H. Wu, and J. M. Yuan, *New J. Phys.* **15**, 045003 (2013).
- [45] P. M. Kowalski, S. Mazevet, D. Saumon, and M. Challacombe, *Phys. Rev. B* **76**, 075112 (2007).
- [46] K. F. Herzfeld, *Phys. Rev.* **29**, 701 (1927).
- [47] J. Rumble, *CRC Handbook of Chemistry and Physics* (CRC Press, Boca Raton, FL, 2017).
- [48] L. Veaser, C. Ekdahl, H. Oona, P. Rodriguez, G. Schmitt, J. Solem, S. Younger, S. Baker, C. Hudson, and W. Lewis, in *Megagauss Magnetic Field Generation, Its Application to Science and Ultra-High Pulsed-Power Technology* (World Scientific, Singapore, 2004), pp. 237–240.
- [49] N. F. Mott and E. A. Davis, *Electronic Processes in Non-crystalline Materials* (Oxford University Press, Oxford, 2012).
- [50] M. Pozzo, M. P. Desjarlais, and D. Alfe, *Phys. Rev. B* **84**, 054203 (2011).
- [51] F. Hensel and W. W. Warren Jr., *Fluid Metals: The Liquid-Vapor Transition of Metals* (Princeton University Press, Princeton, 2014).